Title: Validation of a Fluid-Structure Interaction Numerical Model for Predicting Flow Transients in Arteries.

The authors' full addresses are as follows:

Valentine Kanyanta (first author/corresponding author)
Room 314, Engineering Building
University College Dublin
School of Electrical, Electronics and Mechanical Engineering
Belfiled, Dublin 4
Ireland.

Prof. Alojz Ivankovic (second author)
Professor of Engineering Mechanics
Head of Mechanical Engineering
UCD School of Electrical, Electronic and Mechanical Engineering
Room 228
University College Dublin
Belfield, Dublin 4
Ireland
Tel. +353 (0) 1 716 1994
Fax. +353 (0) 1 283 0534/283 0921

Dr. Aleksandar Karac (third author)
Room 314, Engineering Building
University College Dublin
School of Electrical, Electronics and Mechanical Engineering
Belfiled, Dublin 4
Ireland.

Abstract

The interaction between the flowing blood and deforming arterial wall is critical in understanding the role of hemodynamic forces such as wall shear stress (WSS) in atherosclerosis. Numerical methods have been extensively used to understand the nature of flow around atherosclerosis susceptible regions of the vascular tree in order to establish the exact role of WSS in atherosclerosis. Unfortunately, most of the numerical studies have been performed on rigid arterial geometries, which do not take into account the effect of the interaction between the flowing blood and the dynamics of the flexible arterial wall. *In vivo*, blood vessels are continuously deforming with every contraction and relaxation of the heart during the cardiac cycle.

This paper forms the first of the two-part paper series discussing the need for fluid-structure interaction (FSI) in hemodynamic WSS analysis. The paper presents a well validated FSI based numerical model, capable of accurately predicting flow transients in arteries. The numerical model is validated using analytical solutions and experiments conducted on polyurethane mock artery, with the numerical predictions, analytical solutions and experimental data comparing very well. Numerical studies are performed using OpenFOAM, a 3D Finite Volume Method (FVM) based C++ library.

1. Introduction

Atherosclerosis is a disease of the large arteries involving local accumulation of lipids, calcium and proliferating cells within arterial walls. Although its development has been linked to systematic risk factors such as diabetes, hypertension, and smoking, among others, the non-random occurrence pattern of atherogenic plaques have indicted a strong link between local hemodynamics and the development of atherosclerosis (Malek et al., 1999). Atherosclerotic plaques co-localise with low wall shear stress (WSS) flow regions throughout the vascular tree, from the carotid artery bifurcation (Zarins et al., 1983; Motomiya et al., 1984; Gnasso et al., 1997) to the coronary (Asakura et al., 1990; Friedman et al., 1993), infrarenal and femoral artery vasculatures (Pedersen et al., 1997). WSS is also known to modulate the endothelial phenotype, which contributes to the development of atherosclerosis in the setting of systematic risk factors that enhance the thrombotic, proliferative, and inflammatory components of this pathological process (Malek et al., 1999). High laminar WSS (> 1.5 Pa) induces an atheroprotective gene expression profile, while low WSS (< 0.4 Pa), which is prevalent at atherosclerosis-prone sites, stimulates an atherogenic phenotype.

In order to establish the exact role of WSS in atherosclerosis, an in-depth analysis of flow transients around atherosclerosis susceptible regions of the vascular tree is needed. This can be achieved by use of numerical methods. However, most of the numerical studies in this area are based on rigid, idealised (Steinman et al., 2000; Bertolotti et al., 2000) or patient specific (Steinman et al., 2002; Myers et al., 2001), arterial geometries, were the interaction between the flowing blood and the deforming arterial wall is not taken into account. Though much attention is given to the complex flow pattern around atherosclerosis susceptible regions, the deformation of

the blood vessel during each contraction and expansion of the heart is ignored. In an attempt to resolve this, some studies have used time-varying geometries such as the work of Zeng et al. (2003) and Pivkin et al. (2004). Most recent studies have adopted a FSI approach (Perktold et al., 1995; Marzoa et al., 2005; Yang et al., 2007). However, blood is still modelled as an incompressible fluid, thereby eliminating the effect of propagating waves, which are a key feature of blood flow (Arts et al., 1979; Latham et al., 1985; Zambanini et al., 2005; Millasseau et al., 2005). Most of these models also lack rigorous validation. Therefore, there is need for fully validated fluid-structure interaction (FSI) based numerical models capable of accurate prediction of flow transients in arteries (Ivankovic et al., 2000).

This work takes a combined experimental-numerical approach in order to study the nature of flow in arteries. Experiments are conducted on a straight polyurethane mock artery of inner diameter d = 10 mm and thickness b = 0.5 mm. Tests include pulsatile/unsteady pressure loading of the mock artery and a range of material tests used to determine its mechanical properties (Kanyanta et al., 2008). Flow transients were measured under pulsatile/unsteady pressure loading of the mock artery and used, together with analytical solutions, to validate the numerical model. The numerical model was employed to predict flow transients in the mock artery, using OpenFOAM, a 3D Finite Volume Method (FVM) based C++ library (Wikki Ltd., 2008).

2. Experimental and Numerical Methods

The experimental set-up for the flow experiments was as shown in Fig. 1. The inflow tank is used to provide a pressure head and the solenoid valves (V1 and V2) are used to control the flow through the mock artery. Pulsatile/unsteady flow conditions are achieved by the opening and closing of V1 or V2, which is controlled according to the user-defined control function, taking the

form of the desired pressure waveform (Kanyanta, 2008). The typical pressure waveforms obtained by this method are shown in Fig. 2. Three methods were used in determining pressure wave speed in the mock artery; foot-to-foot, differential pressure and pressure-velocity (PU) loop method.

Foot-to-foot method involves measurement of either pressure or velocity waveforms at two sites, which are a known distance Δx apart along the length of the mock artery. In this case, pressure wave speed C_f is given by

$$C_f = \frac{\Delta x}{\Delta t}, \tag{1}$$

where Δt is the time taken for the wave to travel from one measuring site to the other.

In the differential pressure method, differential pressure between two sites, along the length of the mock artery, and flow rate midway between the two sites, are measured simultaneously. The pressure wave speed is then given by

$$C_f = \frac{\Delta P_{\max}}{\rho_f V_{\max}}, \tag{2}$$

where ΔP_{max} is the maximum differential pressure, V_{max} is the maximum flow velocity and ρ_f is the fluid density.

The theoretical basis of the PU-loop method is the water hammer (Joukowsky) equation, which for backward and forward travelling waves can be expressed as (Khir et al., 2007).

$$dP_{\pm} = \pm \rho_f C_f V \pm . \tag{3}$$

Pressure and velocity (flow rate) are simultaneously measured at a given site along the length of the mock artery. Plotting pressure and velocity over a cycle gives the PU-loop. During the early part of the cycle where only forward travelling waves are hypothesised to be present, the slope of the PU-loop should be linear, and can be given by $S_0 = dP_+ / dV_+ = \rho C_f$.

Fluid velocity was determined from the measured flow rate Q, assuming a turbulent velocity profile given by equation (4), with n = 7, since the flow Wormesley's number (equation (5)), was 13.7 (Kanyanta, 2008), while pressure perturbations were derived from the measured pressure waveforms. Axial stress wave speed and mock artery oscillating frequency could not be determined experimentally due to experimental limitations.

$$V_{\max} = \frac{Q(n+1)(2n+1)}{n^2 2\pi R^2} \tag{4}$$

$$\alpha = r\sqrt{\frac{\rho\omega}{\eta}} \tag{5}$$

Numerical studies were performed using a two-way FSI coupling scheme (Fig. 3) implemented in OpenFOAM (Greenshields et al., 1999; Karac et al., 2003). Here, the fluid and solid parts of the solution domain form separate meshes, but the interface boundary shares the same location in space. The solid and fluid models are combined within a single code and information exchange, in terms of tractions and displacements, takes place at the fluid-solid interface.

Since deformations are small, the solid domain was modelled as a linear elastic solid, using the experimentally determined mechanical properties of polyurethane rubber under wet-room temperature condition (Kanyanta et al., 2008) i.e. E = 5.3 MPa, ρ = 1000 kg/m^2 and ν = 0.4995. The fluid domain was modelled as a compressible Newtonian fluid with dynamic viscosity η = 0.001 Ns/m^2, density ρ_f = 998kg/m^3 and Bulk modulus K = 2.2 GPa (corresponding to the properties of water at 20^{o}C).

3. Mathematical Formulation

The behaviour of a continuum in Eulerian frame reference is governed by the following equations (neglecting body forces)

- Mass balance, or continuity equation

$$\frac{\partial \rho}{\partial t} + \nabla \cdot (\rho \mathbf{V}) \tag{6}$$

- Momentum balance, or Cauchy's first law of motion

$$\frac{\partial \rho \mathbf{V}}{\partial t} + \nabla \cdot (\rho \mathbf{V}\mathbf{V}) = \nabla \cdot \boldsymbol{\sigma}, \tag{7}$$

where ρ is the density, **V** is the velocity, and **σ** is the stress tensor. The constitutive laws for a linear elastic (Hookean) solid and Newtonian fluid are

- Stress-strain relation for a Hookean solid

$$\boldsymbol{\sigma} = 2\mu + \lambda tr(\boldsymbol{\varepsilon})\mathbf{I} \tag{8}$$

- Stress-strain rate relation for a Newtonian fluid (Stokes's law)

$$\boldsymbol{\sigma} = 2\eta\dot{\boldsymbol{\varepsilon}} - \frac{2}{3}\eta tr(\dot{\boldsymbol{\varepsilon}})\mathbf{I} - p\mathbf{I}, \tag{9}$$

where μ and λ are Lame' coefficients, $\boldsymbol{\varepsilon} = \frac{1}{2}\left[\nabla \mathbf{U} + (\nabla \mathbf{U})^T\right]$ is the strain tensor, **U** is the displacement vector, **I** is the identity tensor, η is the dynamic viscosity, $\dot{\boldsymbol{\varepsilon}} = \frac{1}{2}\left[\nabla \mathbf{V} + (\nabla \mathbf{V})^T\right]$ is the deformation rate, and p is the hydrostatic pressure.

In the case of a linear elastic solid, the continuity equation need not to be considered and since the deformations are sufficiently small, the convection term $\nabla \cdot (\rho \mathbf{V}\mathbf{V})$ can be neglected and **V** becomes $\partial \mathbf{U}/\partial t$, and the analysis in the Eulerian and Lagrange formulations are almost identical. A single equation can then be derived for the structure (solid domain) in terms of **U** as in equation (10)

$$\frac{\partial}{\partial t}\left(\rho \frac{\partial \mathbf{U}}{\partial t}\right) = \nabla \cdot \left[\mu \nabla \mathbf{U} + \mu(\nabla \mathbf{U})^T + \lambda \mathbf{I} tr(\nabla \mathbf{U})\right]. \tag{10}$$

For the fluid flow, both the continuity equation and the momentum balance must be satisfied and the convection term cannot be ignored. The momentum balance, in terms of velocity **V**, hence becomes

$$\frac{\partial (\rho \mathbf{V})}{\partial t} + \nabla \cdot (\rho \mathbf{V}\mathbf{V}) = \nabla \cdot \eta\left[\nabla \mathbf{V} + (\nabla \mathbf{V})^T - \frac{2}{3}\mathbf{I} tr(\nabla \mathbf{V})\right] - \nabla p. \tag{11}$$

The system of fluid equations is closed by relating pressure and density of compressible liquids by bulk modulus K

$$K = \rho \frac{\partial p}{\partial \rho}. \tag{12}$$

For small values of ρ/ρ_0 (low pressures), equation (12) can be expressed via the well known barotropic equation

$$\rho = \rho_0 + \psi(p - p_0), \text{ where } \psi = \frac{\rho_0}{K}, \tag{13}$$

and the subscript 0 represents reference values.

The Pressure Implicit with Splitting of Operators (PISO) algorithm is used to solve the discretised pressure-velocity coupled equations.

Since FVM is based on numerical integration of the system of equations over a computational domain, the time domain is discretized into a finite number of time steps and the spatial domain subdivided into a finite number of contiguous control volumes or cells. Dependent variables and material properties are stored at cell centroids. Numerical integration employs the mid-point rule and linear interpolation of the dependent variables between the cell centroids is assumed. Full details of the discretisation procedure are presented in (Greenshields et al., 1999).

4. Numerical Model Validation

The numerical model was validated by comparing its predictions of flow transients in a straight water-filled polyurethane mock artery to analytical solutions and experimental data. The problem definition is shown in Fig. 4. The problem is axi-symmetric and therefore only required a solution domain in 2D. The optimum mesh used had 800 cells along the pipe length, 40 cells across the fluid domain and 4 cells across the solid domain. Wave propagation was initiated at the left end of the pipe by applying a fixed step change in pressure of p = 7.5 kPa. Each analysis was run using a

time step to ensure Courant < 1. The left and right pipe wall boundaries were treated as planes of symmetry and the outer wall had zero traction boundary condition. The fluid inlet boundary was fixed pressure and zero velocity gradient while the outlet was a plane of symmetry. Structure displacements were solved using the Incomplete-Cholesky Conjugate Gradient (ICCG) method to a tolerance of 10^{-8}. The Incomplete-Cholesky Biconjugate Gradient (BICCG) method was used for fluid velocity **V** and pressure p due to the asymmetric nature of the coefficient matrix of the system of discretised equations. **V** and p were solved to tolerances of 10^{-5} and 10^{-6}, respectively.

4.1. Analytical solutions

In a straight unconstrained section of a pipe, the analytical solution of pressure wave speed C_f is given by (Wylie et al., 1993)

$$C_f = \sqrt{\frac{K}{\rho_f}\left[1+\left(\frac{(d+2b)^2}{b(d+b)}-2(1-\nu)\right)\frac{K}{E}\right]^{-1}} \quad . \tag{14}$$

Equation (14) only accounts for the change in pipe area, and assumes axial stress to be fixed over the entire pipe length. This results in an overestimation in wave speed. A better solution is obtained by applying a factor φ that accounts for the axial stress waves in the pipe wall.

$$\varphi = \sqrt{1-\nu^2\left[1+\frac{E}{K}\left(\frac{b}{d}\right)\left(1-\frac{K\rho_f}{E\rho_s}\right)\right]^{-1}} \quad . \tag{15}$$

The corrected analytical solution for pressure wave speed then becomes

$$\widetilde{C}_f = \varphi C_f \, . \tag{16}$$

The stress wave (precursor wave) speed for an infinitely long plate is given by

$$C_s = \sqrt{\frac{E}{\rho_s}} \, , \tag{17}$$

and for a thin plate by

$$\widetilde{C}_s = \sqrt{\frac{E}{\rho_s\left(1-\nu^2\right)}}. \tag{18}$$

The relationship between pressure and velocity under unsteady, unidirectional flow is governed by the water hammer equation

$$V_x = \frac{\Delta p}{\rho_f C_f}, \tag{19}$$

where Δp is the pressure difference across the wavefront and V_x is the axial flow velocity.

Three coupling mechanisms exist in FSI: Poisson coupling, friction coupling, and junction coupling. Poisson coupling is associated with hoop stress perturbations produced by fluid pressure transients that results in axial stress perturbations through Poisson ratio coefficient. The axial stress and accompanying axial strain perturbations travel as waves in the pipe wall at approximately the speed of sound in a solid plate (equation 17). Friction coupling is created by shear stress transients acting on the pipe wall, which is usually insignificant compared to the other two coupling mechanisms. Junction coupling results from the reactions of unbalanced pressure forces and changes in liquid momentum at specific points along the pipe such as bends, tees, valves etc. Only Poisson coupling effects are discussed in this paper since the work involves flow transients in a straight pipe and friction coupling effects are assumed negligible.

The relationships between axial stress perturbations caused by pressure transients and vice-versa, are given by (Wiggert et al., 2001)

$$\Delta\boldsymbol{\sigma} = -G_s \Delta p \ \text{ and } \ \Delta p = -G_f \Delta\boldsymbol{\sigma}, \tag{20}$$

where G_f and G_s are the fluid and solid coupling factors, respectively, given by

$$G_f = -2\nu\frac{\rho_f}{\rho_s}\left[\left(\frac{C_s}{\widetilde{C}_f}\right)^2 - 1\right]^{-1} \ \text{ and } \ G_s = 2\nu\frac{r}{b}\left[\left(\frac{\widetilde{C}_s}{C_f}\right)^2 - 1\right]^{-1}, \tag{21}$$

and r is the pipe radius. $\widetilde{C}_f$ and $\widetilde{C}_s$ are the modified pressure and axial stress wave speeds, given

by equations (16) and (18), respectively.

Equation (20) shows the importance of FSI. Poisson coupling effects increase as the wall stiffness decrease (equation (21)).

Flow transients also include the pipe's natural oscillating frequency.

5. Results

5.1. Numerical Model Validation

Numerical predictions of flow transients in a water-filled polyurethane mock artery were compared with analytical solutions and experimental data in order to validate the numerical model.

5.1.1. Pressure Wave Speed, Deformations and Oscillating frequency

Numerical simulation predicts wave propagation along the mock artery as presented in Fig. 5(a). Figures 5(b), 6(a) and 6(b) show the experimental determination of pressure wave speed using the foot-to-foot, differential pressure and PU loop methods, respectively. The analytical solution of pressure wave speed is determined by equation (16), and is equal to 13.31 m/s, while the average experimental value is 13.14 m/s. The simulated value (Fig. 5(a)) is 13.25 m/s, which is 0.4% lower and 0.8% higher than the analytical solution and experimental value, respectively. Fig. 7 shows the comparison between the simulated and analytical solutions for pressure wave speed over a wide range of Young's modulus values.

The other important feature of wave propagation is radial wall deformation shown in Fig. 8(a), with radial displacement of 0.076mm, which is close to the analytical value approximated by $(d+b)^2\ p/4Eb$ = 0.078 mm. The comparison between the numerical prediction of mock artery

deformations and experimental data is widely covered in (Quinn et al., 2008).

The results also show noticeable oscillations in the wall deformations ahead of the pressure wavefronts (Fig. 8(a)). The averaged simulated wavelength for the first oscillation, for t = 4.8ms, is ≈ 0.073m. Using equation (18), the estimated natural frequency becomes 1084Hz. The analytical solution for the pipe's natural frequency is the ring frequency of a freely vibrating hoop, equation (22). It is derived from the pipe circumferential stiffness, its mass, and an equivalent mass of the fluid and is given by

$$f = \frac{1}{2\pi r}\sqrt{\frac{4E}{\rho_s + \alpha\frac{r}{b}\rho_f}}, \qquad (22)$$

where the coefficient α determines the added fluid mass M_f.

In the literature values of α of 1/4, 1/3 and 1/2 have been proposed, depending on the assumed distribution of the radial fluid velocity (Tijsseling et al., 2006).

$$\alpha = \begin{cases} \frac{1}{2} & for\ M_f, "A" = the\ total\ mass\ of\ the\ fluid \\ \frac{1}{3} & for\ M_f, "B" = 2/3\ of\ the\ total\ mass\ of\ the\ fluid \\ \frac{1}{4} & for\ M_f, "C" = 1/2\ of\ the\ total\ mass\ of\ the\ fluid \end{cases} \qquad 23)$$

Using equation (22) and equivalent fluid mass M_f in equation (23), the analytical solutions for the frequency are 947Hz, 1112Hz, and 1237Hz for M_f = A, B, and C respectively. Compared to the simulated frequency, these values are, respectively, 17%, 2% lower and 9% higher. The values obtained using M_f = B and M_f = C are closer to the numerical value than for M_f = A. This indicates that only a fraction of the total mass of the fluid contributes to radial deformation. Alternative solutions B and C are based on a linear distribution of radial flow velocity and the validity of this assumption is confirmed by the simulation results presented in Fig. 9(b).

The frequency decreases with time as shown in Fig. 8(b). This is because the pipe is axially constrained at its two ends. Hence as the wavefront advances, the simulated frequency deviates from the analytically predicted value(s). The analytical solutions are for the instant when the pipe is fully deformed (i.e. t = 4.8ms).

5.1.2. Fluid Particle Velocity

Fig. 9(a) presents numerical and analytical predictions of fluid particle flow speed Vx along the pipe centreline, showing good comparison between the two data sets over the entire length of the pipe.

The experimentally determined axial velocity, at a pressure of 7.5kPa, was 0.46 m/s (Kanyanta, 2008), which is about 8% lower than the analytical and simulated values of approximately 0.5 m/s.

The radial fluid velocity varies linearly with radial distance as shown in Fig. 9(b). At the interface, the normal (radial) component of the fluid velocity is equal to that of the solid wall and the axial component is zero.

5.1.3. Poisson Coupling Effects

Stress waves in the solid domain are initiated by the sudden increase in fluid pressure at the fluid inlet (Fig. 4). These waves travel along the pipe length at the speed of sound through a solid plate (equation (18)), which in this case is about 6 times faster than the pressure wave speed.

Axial stress waves (Fig. 10(b)) produce pressure perturbations Δp, also known as precursor waves, as shown in Fig. 10(a). Similarly, pressure transients (Fig. 10(a)) produce axial stress perturbations $\Delta\sigma$ shown in Fig. 10(b). Axial stress and pressure perturbations propagate along the length of the pipe at same speeds as the pressure and axial stress waves, respectively.

The magnitude of pressure perturbations, Δp, and axial stress perturbations, $\Delta\sigma$, are about 14.3% and 13.4% of the primary pressure waves (Fig. 10(a)) and axial stress waves (Fig. 10(b)), respectively. Numerical and analytical values of Δp are 1070Pa and 1050Pa, and for $\Delta\sigma$ are −2350Pa and −2250Pa, respectively. The experimentally determined magnitude of Δp, corresponding to a change in pressure of 7.5 kPa, was 1200 Pa (Kanyanta, 2008), making the numerical value of Δp 2% higher and 12% lower than the analytical solution and experimental data, respectively, and that of $\Delta\sigma$ 4% higher than its analytical solution.

The numerical value of the axial stress wave speed (Fig. 10(b) i.e. $C_s = \Delta x/\Delta t$) is 86.25 m/s and its analytical solution is 84 m/s.

Overall, the numerical model gives a very good prediction of flow transients in a straight water-filled polyurethane mock artery.

6. Discussion and Conclusion

The precise prediction of blood flow through a flexible artery requires appropriate fluid-structure coupling because of the importance of the interaction between the flowing blood and the deforming arterial wall in the study of blood flow transients. The numerical model was validated by comparing its predictions for flow transients in a water-filled polyurethane mock artery to the analytical solutions and experimental data. Flow parameters such as pressure and axial stress (or precursor) wave speeds, wall deformations and oscillating frequency, fluid flow velocity, and Poisson coupling effects, were used as the basis of this validation. The results showed very good comparison between numerical prediction, analytical solutions and experimental data, with over 95% agreement between the three data sets. Therefore, this work presents a well validated numerical model, capable of accurate prediction of flow transients in arteries, via FSI analysis.

Acknowledgements

www.wikki.co.uk

This work is supported by Science Foundation Ireland

References

Malek, M.A., Alper, L.S., Izumo, S., 1999. Hemodynamic shear stress and its role in atherosclerosis. JAMA 282(21), 2035-2042.

Zarins, C.K., Giddens, D.P., Bharadvaj, B.K., Sottiurai, V.S., Mabon, R.F., Glagov, S., 1983. Carotid bifurcation atherosclerosis. Quantitative correlation of plaque localization with flow velocity profiles and wall shear stress. Circulation Research 53, 502-514.

Motomiya, M. and Karino, T., 1984. Flow Patterns in the Human Carotid Artery Bifurcation. Stroke 15(1), 50-56.

Gnasso, A., Irace, C., Carallo, C., Serena De Franceschi, M., Motti, C., Mattioli, L.P., Pujia, A., 1997. *In vivo* association between low wall shear stress and plaque in subjects with asymmetrical carotid atherosclerosis. Stroke 28, 993-998.

Asakura, T. and Karino, T.,1990. Flow patterns and spatial distribution of atherosclerotic lesions in human coronary arteries. Circulation Research 66, 1045-1066.

Friedman, M.H., Brinkman, A.M., Qin, J.J., Seed, W.A.,1993. Relation between coronary artery geometry and the distribution of early sudanophilic lesions. Atherosclerosis 98(2), 193-199.

Pedersen, E.M., Agerbaek, M., Kristensen, I.B., Yoganathan, A.P., 1997. Wall shear stress and early atherosclerotic lesions in the abdominal aorta in young adults. Vascular and Endovascular Surgery 13, 443-451.

Steinman, D.A., Poepping, T.L., Tambasco, M., Rankin, R.N., Holdsworth, D.W., 2000. Flow

patterns at the stenosed carotid bifurcation: Effects of concentric versus eccentric stenosis. Annals of Biomedical Engineering 28(4), 415-423.

Bertolotti, C., Deplano, V., 2000. Three-dimensional numerical simulations of flow through a stenosed coronary bypass. Journal of Biomechanics 33, 1011-1022.

Steinman, D.A., Thomas, J.B., Ladak, H.M., Milner, J.S., Rutt, B.K., Spence, J.D., 2002. Reconstruction of carotid bifurcation hemodynamics and wall thickness using computational fluid dynamics and MRI. Magnetic Resonance in Medicine 47(1), 149-159.

Myers, J.G., Moore, J.A., Ojha, M., Johnston, K.W., Ethier, C.R., 2001. Factors influencing blood flow patterns in the human right coronary artery. Annals of Biomedical Engineering 29(2), 109-120.

Zeng, D., Ding, Z., Friedman, M.H., Ethier, C.R., 2003. Effects of cardiac motion on right coronary artery hemodynamics. Annals of Biomedical Engineering 31, 420-429.

Pivkin, I., Richardson, P., Laidlaw, D., Karniadakis, G., 2004. Effects of cardiac motion on right coronary artery hemodynamics. Journal of Biomechanics 38(6), 1283-1290.

Yang, X.L., Liu, Y., Yang, J. M., 2007. Fluid-structure interaction in a pulmonary arterial bifurcation. Journal of Biomechanics 40(12), 2694-2699.

Marzoa, A., Luob, X.Y., Bertramc, C.D., 2005. Three-dimensional collapse and steady flow in thick-walled flexible tubes. Journal of Fluids and Structures 20(6), 817-835.

Perktold, K., Rappitsch, G., 1995. Computer simulation of local blood flow and vessel mechanics in a compliant carotid artery bifurcation model. Journal of Biomechanics 28(12), 845-856.

Zambanini, A., Cunningham, S.L., Parker, K.H., Khir, A.W., McG. Thom, S.A., Hughes, A.D., 2005. Wave-nergy patterns in carotid, brachial, and radial arteries: a non-invasive approach using

wave-intensity analysis. American Journal of Physiology: Heart and Circulatory Physiology 289, H270-H276.

Arts, T., Kruger, R.T., van Gerven, W., Lambregts, J.A., Reneman, R.S., 1979. Propagation velocity and reflection of pressure waves in the canine coronary artery. Heart and Circulatory Physiology 237(4), H469-H474.

Millasseau, S.C., Stewart, A.D., Patel, S.J., Redwood, S.R., Chowienczyk, P.J., 2005. Evaluation of carotid-femoral pulse wave velocity. Hypertension 45, 222-226.

Latham, R.D., Westerhof, N., Spikema, P., Rubal, B.J., Reuderink, P., Murgo, J.P., 1985. Regional wave travel along the human aorta: a study with six simultaneous micromanometric pressures. Circulation 72, 1257-1269.

Khir, A. W., Swalen, M. J. P., Feng, J., Parker, K. H., 2007. Simultaneous determination of wave speed and arrival time of reflected waves using the pressure-velocity loop. Medical and Biological Engineering and Computing 45, 1201-1210.

Greenshields, C.J., Weller, H.G., Ivankovic, A., 1999. The finite volume method for coupled fluid flow and stress analysis. Computational Modelling and Simulation in Engineering 4, 213-218.

Kanyanta, V., Ivankovic, A., 2008. Mechanical charaterisation of polyurethane rubber for biomedical applications (in preparation). Journal of Biomechanics

Ivankovic, A., Karac, A., Dendrinos, E., Parker, K., 2000. Towards early diagnosis of atherosclerosis: The finite volume method for fluid-structure interaction. Biorheology 39, 401-407.

Wiggert, D.C., Tijsseling, A.S., 2001. Fluid transients and fluid-structure interaction in flexible liquid-filled piping. Applied Mechanics Reviews 54, 456-481.

Karac, A., Ivankovic, A., 2003. Modelling the drop impact behaviour of fluid-filled

polyethylene containers. Fracture of Polymers, Composites and Adhesives II 32, 253-264. ESIS Publication, Elsevier Ltd.

www.wikki.co.uk. Open source CFD solution for research and industry

Wylie, E.B. and Streeter, V.L., 1993. Fluid transients in systems. Prentice Hall, Englewood Cliffs, New York.

Tijsseling, A.S., Lambert, M.F., Simpson, A.R., Stephens, M.L., Vtkovsk, J.P., Bergant, A., 2006. Wave front dispersion due to fluid-structure interaction in long liquid-filled pipelines. In Proceedings 23rd IAHR Symposium on Hydraulic Machinery and Systems, Yokohama, Japan, October 17-21, 2006. Engineering in Medicine and Biology Society. Paper 143 IAHR.

Quinn, N., Ivankovic, A., 2008. Towards early diagnosis of atherosclerosis: The effect of thickening and stiffening on the deformation profiles of polyurethane mock arteries (in preparation). Journal of Biomechanics.

Kanyanta, V., 2008. Towards early diagnosis of atherosclerosis: wall shear prediction. PhD thesis, University College Dublin, Ireland.

Kamiya, A., Bukhari, R., Togawa, T., 1984. Adaptive regulation of wall shear stress optimising vascular tree function. Bulletin of Mathematical Biology 46, 127-137.

Riley, W.A., Barnes, R.W., Evans, G.W., Burke, L.G., 1992. Ultrasonic measurement of the elastic modulus of the common carotid artery. The atherosclerosis risk in communities (ARIC) study. Stroke 23, 952-956

Figure(s)

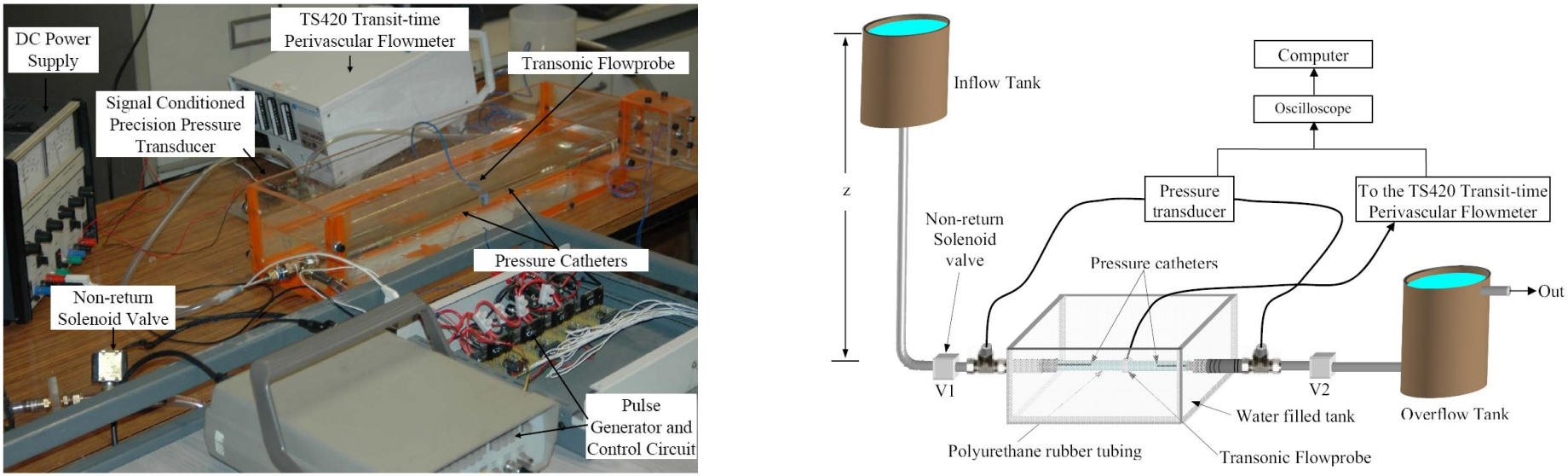

(a) (b)

Figure 1: (a) Experiment set-up and (b) schematic of the experimental set-up, for flow transients in a straight water filled polyurethane mock artery.

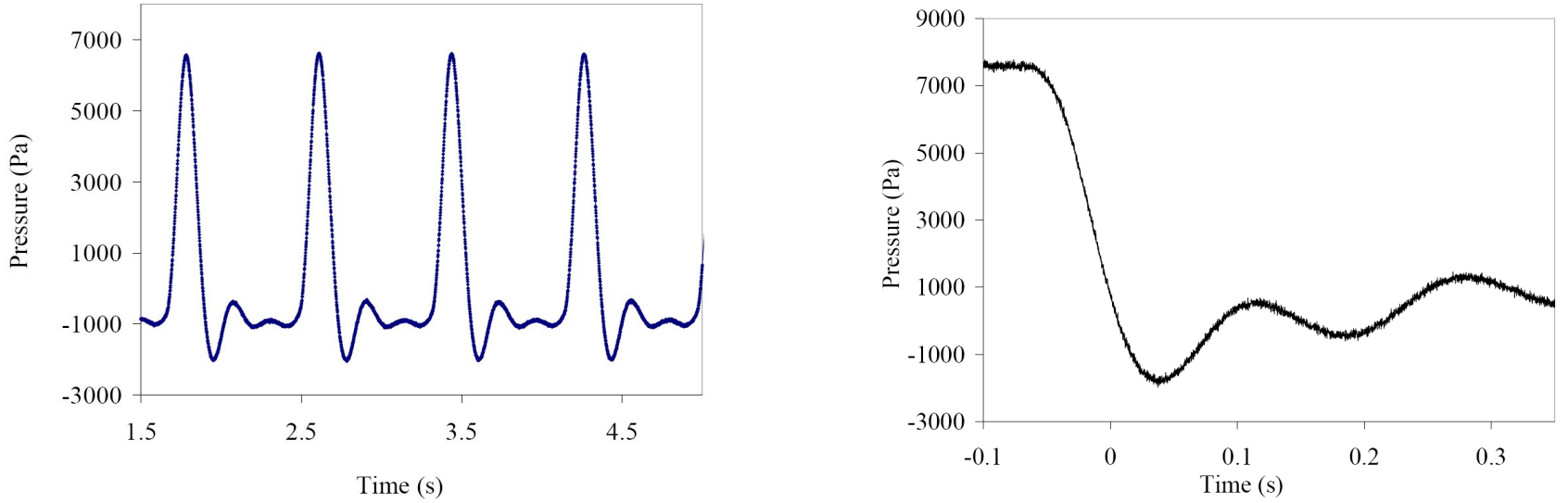

(a) (b)

Figure 2: Typical pressure waveform(s) generated experimentally: (a) pulsatile and (b) sudden valve (V2) opening.

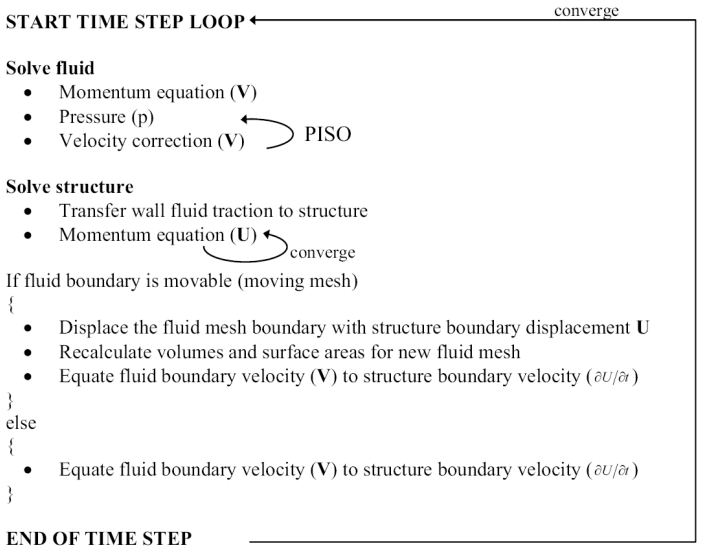

Figure 3: Implicit solution scheme for fluid-structure interaction (Greenshields et al., 1999).

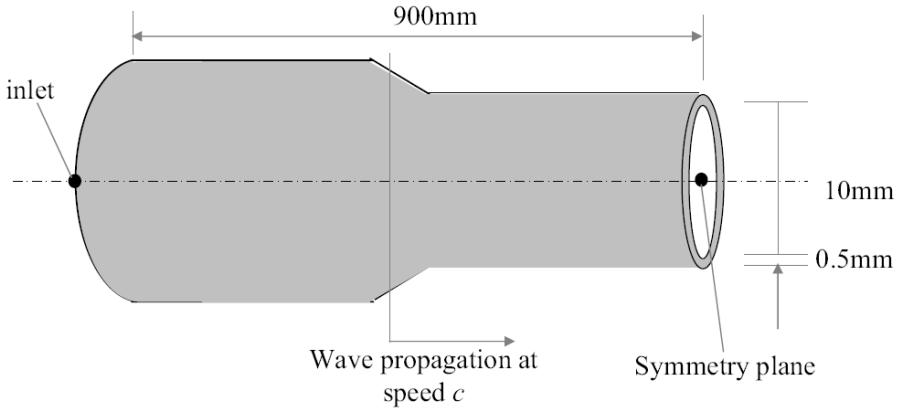

Figure 4: Problem description.

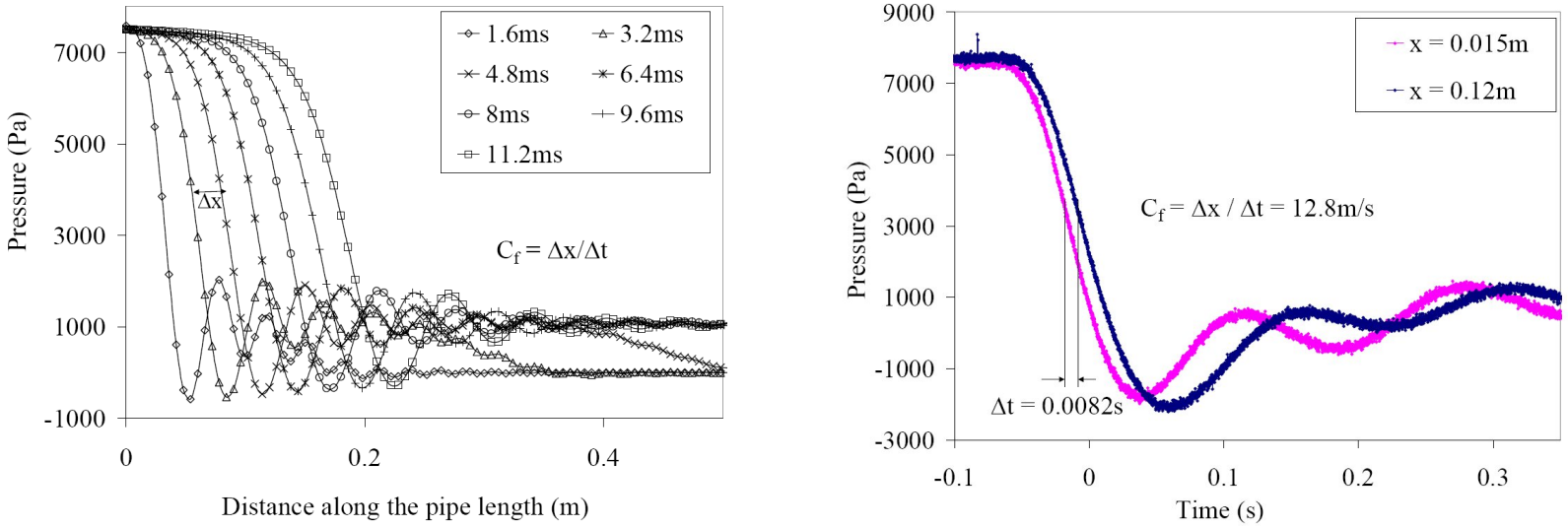

(a) (b)

Figure 5: Pressure wave speed determination using (a) numerical method and (b) experimental foot-to-foot method.

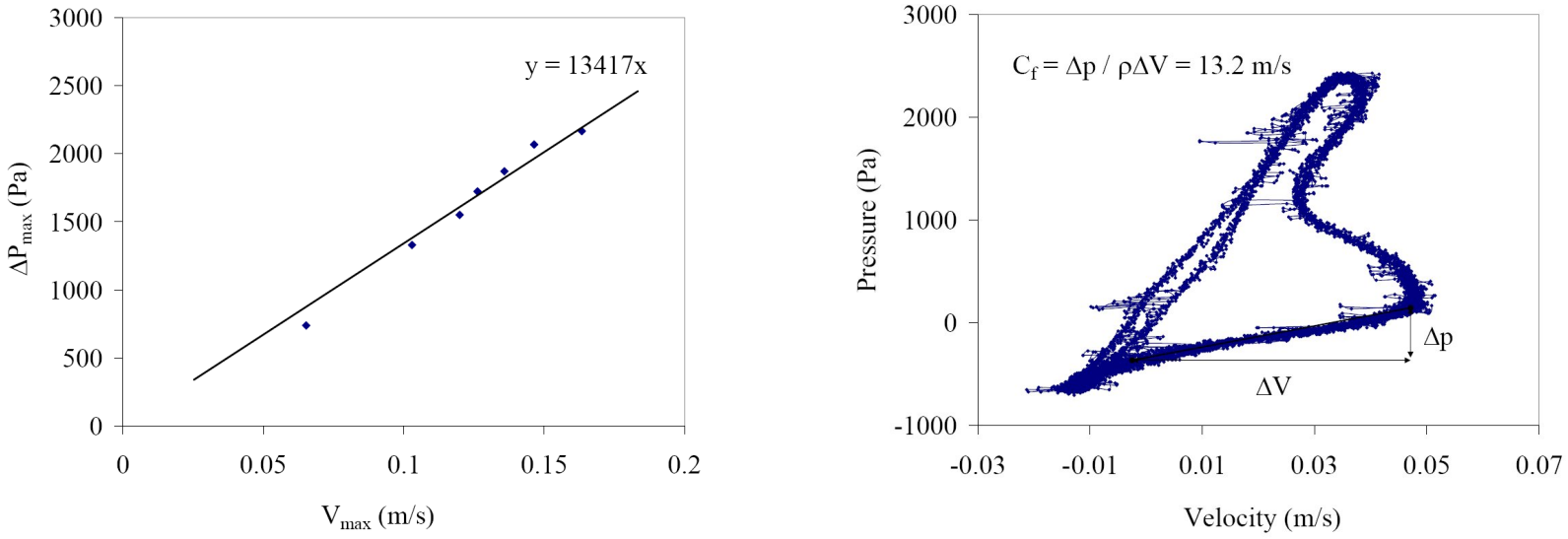

(a) (b)

Figure 6: Pressure wave speed determination using experimental (a) differential pressure and (b) PU loop methods.

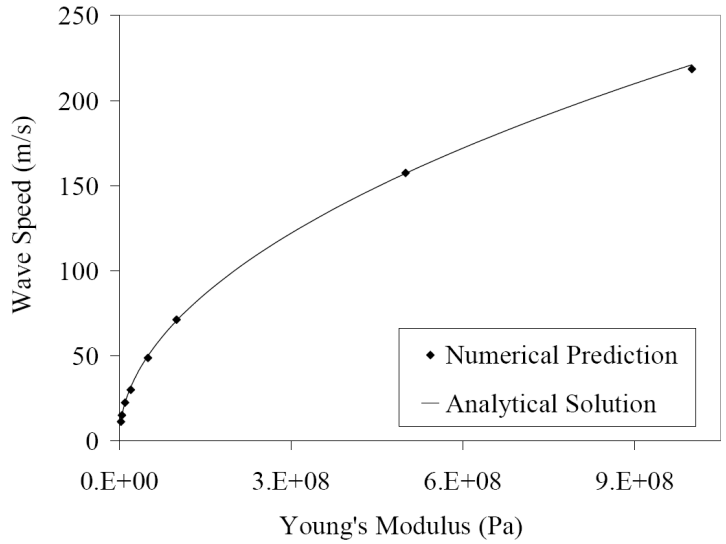

Figure 7: Predicted pressure wave speed with increasing pipe stiffness.

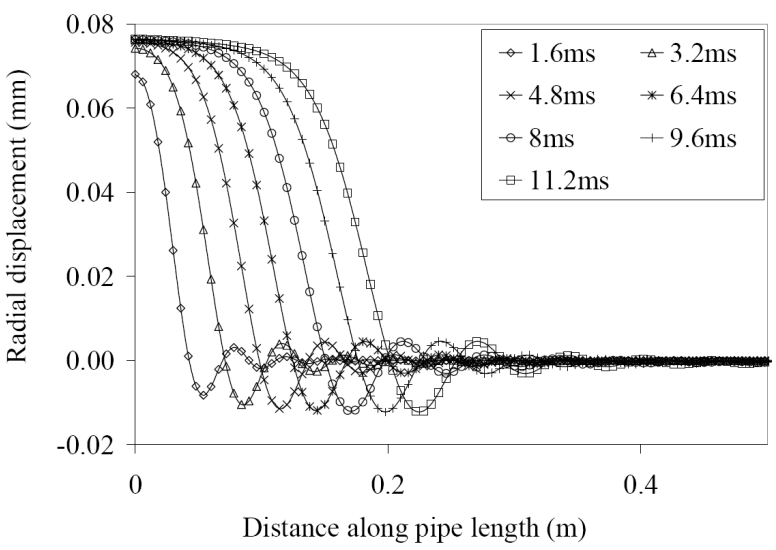

(a)

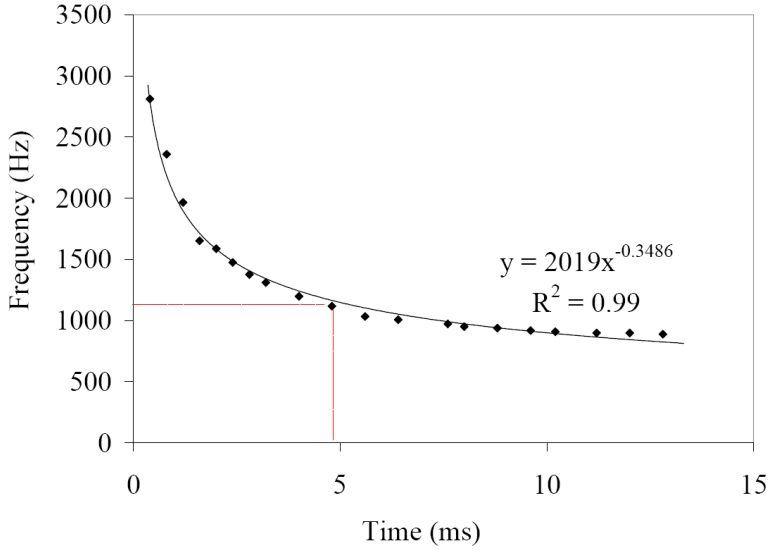

(b)

Figure 8: (a) Radial wall displacement at different time intervals (taken from the mid-wall section) and (b) wall oscillating frequency.

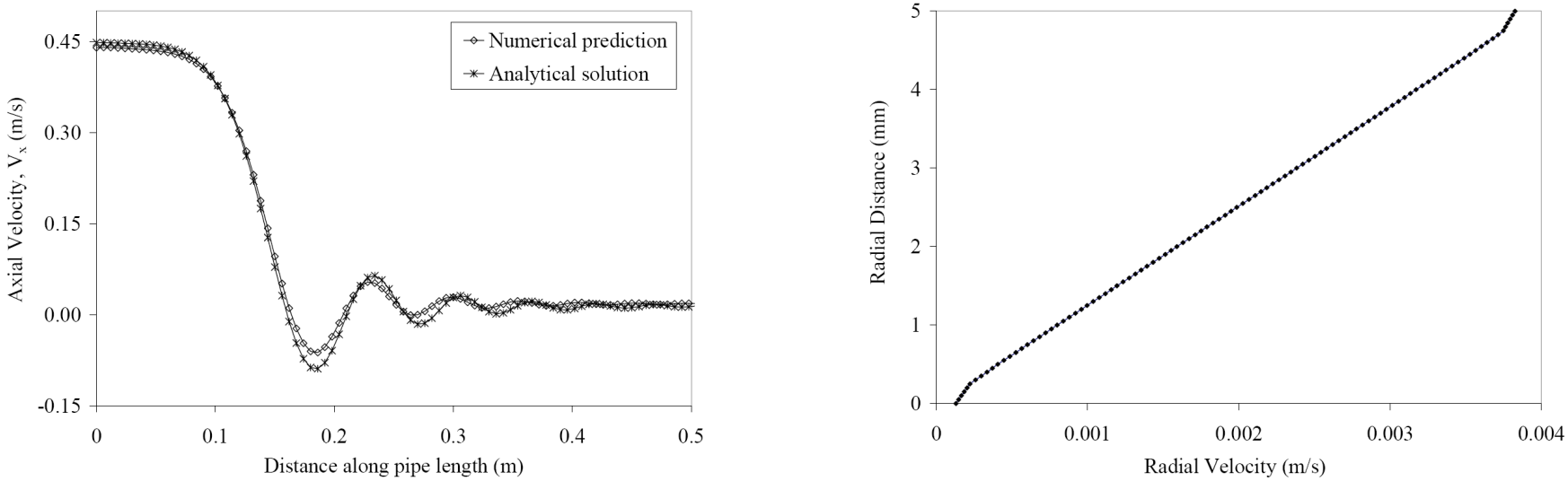

(a) (b)

Figure 9: Comparison between numerical and analytical prediction of (a) axial flow velocity along the mock artery centreline and (b) radial component of fluid velocity field at 80mm from the mock artery inlet.

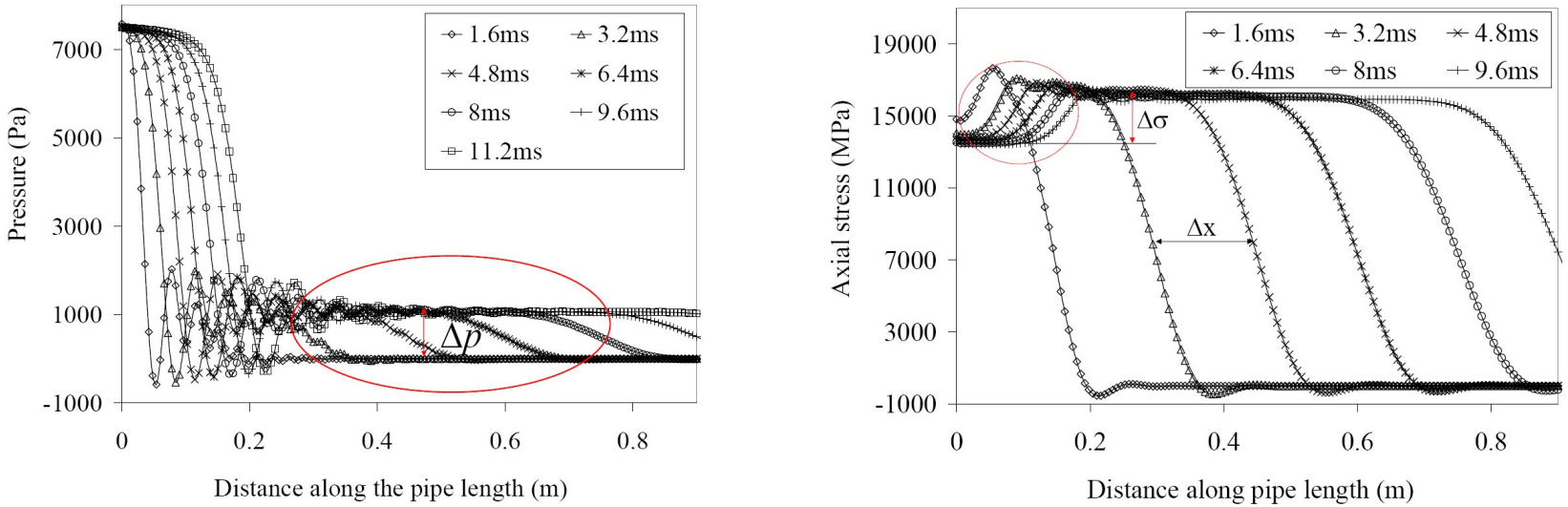

(a) (b)

Figure 10: (a) Pressure perturbations caused by axial stress transients and (b) axial stress perturbations caused by pressure transients.

Conflict of Interest Statement

This work is supported by Science Foundation Ireland and all the work presented was conducted at University College Dublin